




Open Archive Toulouse Archive Ouverte (OATAO)

OATAO is an open access repository that collects the work of Toulouse researchers and makes it freely available over the web where possible

This is an author's version published in: <http://oatao.univ-toulouse.fr/19800>

Official URL: <https://doi.org/10.1021/acs.jpcllett.7b03315>

To cite this version:

Torayev, Amangeldi and Rucci, Alexis and Magusin, Pieter C. M. M. and Demortière, Arnaud and De Andrade, Vincent and Grey, Clare P. and Merlet, Céline  and Franco, Alejandro A. *Stochasticity of Pores Interconnectivity in Li-O₂ Batteries and its Impact on the Variations in Electrochemical Performance*. (2018) The Journal of Physical Chemistry Letters, 9 (4). 791-797. ISSN 1948-7185

Any correspondence concerning this service should be sent to the repository administrator: tech-oatao@listes-diff.inp-toulouse.fr

Stochasticity of Pores Interconnectivity in Li–O₂ Batteries and its Impact on the Variations in Electrochemical Performance

Amangeldi Torayev,^{†,‡,§} Alexis Rucci,^{†,||} Pieter C. M. M. Magusin,^{‡,§} Arnaud Demortière,^{†,‡,||} Vincent De Andrade,[⊥] Clare P. Grey,^{‡,§} Céline Merlet,^{§,||,#} and Alejandro A. Franco^{*,†,‡,||,∇}

[†]Laboratoire de Réactivité et Chimie des Solides (LRCS), CNRS UMR 7314, Université de Picardie Jules Verne, HUB de l'Énergie, Rue Baudelocque, 80039 Amiens, France

[‡]ALISTORE-European Research Institute, FR CNRS 3104, HUB de l'Énergie, Rue Baudelocque, 80039 Amiens, France

[§]Department of Chemistry, University of Cambridge, Lensfield Road, Cambridge CB2 1EW, United Kingdom

^{||}Réseau sur le Stockage Electrochimique de l'Énergie (RS2E), FR CNRS 3459, HUB de l'Énergie, Rue Baudelocque, 80039 Amiens, France

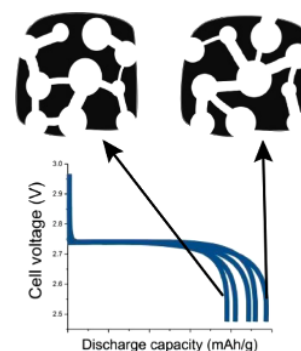
[⊥]X-Ray Science Division, Advanced Photon Source, Argonne National Laboratory, Lemont, Illinois 60439, United States

[#]CIRIMAT, Université de Toulouse, CNRS, INPT, UPS, Université Toulouse 3 Paul Sabatier, Bât. CIRIMAT, 118, route de Narbonne, 31062 Toulouse cedex 9, France

[∇]Institut Universitaire de France, 103 Boulevard Saint-Michel, 75005 Paris, France

Supporting Information

ABSTRACT: While large dispersions in electrochemical performance have been reported for lithium oxygen batteries in the literature, they have not been investigated in any depth. The variability in the results is often assumed to arise from differences in cell design, electrode structure, handling and cell preparation at different times. An accurate theoretical framework turns out to be needed to get a better insight into the mechanisms underneath and to interpret experimental results. Here, we develop and use a pore network model to simulate the electrochemical performance of three-dimensionally resolved lithium–oxygen cathode mesostructures obtained from TXM nanocomputed tomography. We apply this model to the 3D reconstructed object of a Super P carbon electrode and calculate discharge curves, using identical conditions, for four different zones in the electrode and their reversed configurations. The resulting galvanostatic discharge curves show some dispersion, (both in terms of capacity and overpotential) which we attribute to the way pores are connected with each other. Based on these results, we propose that the stochastic nature of pores interconnectivity and the microscopic arrangement of pores can lead, at least partially, to the variations in electrochemical results observed experimentally.



Since Abraham and Jiang demonstrated the first proof of concept of an aprotic Li–O₂ battery, there has been a significant interest due to its superior theoretical capacity (5.2 kWh·kg⁻¹) compared to state of the art Li-ion batteries.^{1,2} In the last two decades numerous aspects of Li–O₂ batteries have been investigated. Research efforts have demonstrated how the positive electrode mesostructure affects the cell capacity,^{3–6} the influence of the electrolyte stability and its contribution to the cell performance,^{7,8} and the use of mediators to favor formation of large discharge particles.^{9–11} There has been a wide range of capacities reported in the literature, going from a few hundreds of mAh·g⁻¹^{4,12} to 29 375 mAh·g⁻¹ for catalyzed porous graphene nanostructures,¹³ and 37 523 mAh·g⁻¹ for carbon electrodes with tailored architectures.¹⁴ These works use different types of carbons and operating conditions. However, even if only a single parameter is altered, the results can differ significantly. Meini et al. reported that the discharge capacities of Ketjenblack EC600JD and Black Pearls 200 increase from around 438 mAh·g⁻¹ and 517 mAh·g⁻¹ to 1833 mAh·g⁻¹ and 2168 mAh·g⁻¹, respectively, when simply replacing the

diethylene glycol dimethyl ether solvent by the tetraethylene glycol dimethyl ether solvent.⁴ As shown by Read, simply using different pressing methods during electrode preparation can affect the discharge capacity significantly.¹⁵ In his work, a Super P-based electrode with PTFE binder is prepared by hot and cold pressing methods, and the discharge capacity obtained for the hot pressing approach is 1347 mAh·g⁻¹, while a capacity of 2120 mAh·g⁻¹ is achieved for the cold pressed one. All these studies have shown that Li–O₂ batteries are extremely sensitive to operating conditions and cell components.

The sensitive nature of Li–O₂ batteries leads to a non-negligible dispersion of experimental results. Griffith et al. reported reproducibility tests for 60 cells at 5 different current densities via well-controlled experimental procedures, yet still a large variation of discharge capacities was observed.¹⁶ The

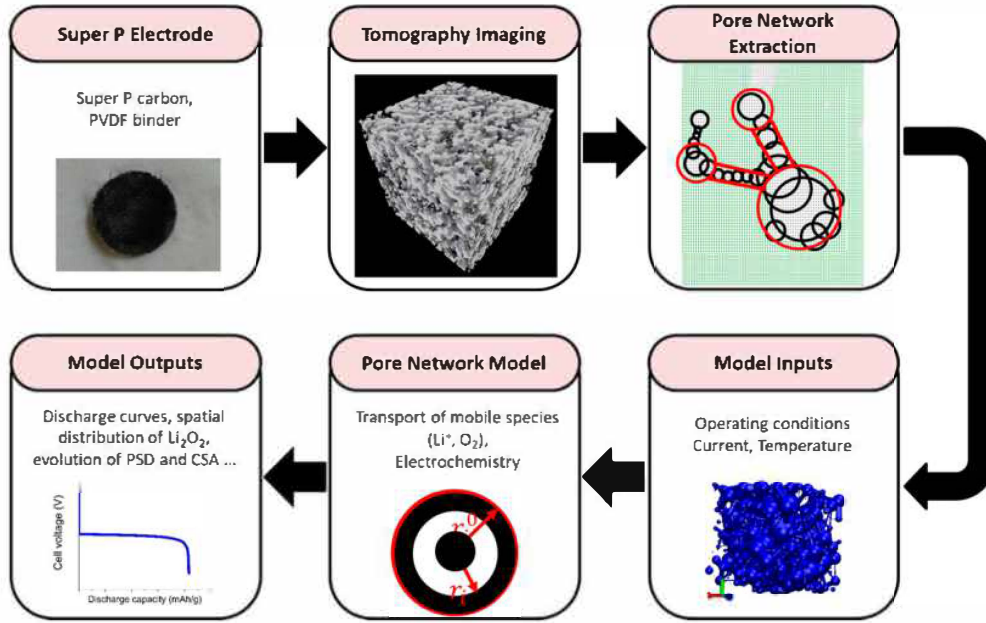


Figure 1. Workflow of our modeling approach.

dispersion of results is observed in experiments, but insufficient attention is paid to the origin of this phenomenon. It is often assumed to result from the uncertainty in the material quantities (e.g., mass loading, electrolyte amount), handling issues or variations from one experiment to another.

On the modeling side, the common approach to study Li–O₂ batteries is to use continuum models and to capture the effects of pores interconnectivity via a tortuosity factor. The tortuosity is usually described via the Bruggeman relationship, which oversimplifies the role of pore sizes and connectivity on transport.^{17–19} Recently, Mehta et al. showed, for the first time, that the local variation of porosity and carbon surface area (CSA) in the cathode can lead to variations in performance as well.²⁰ In their model, the positive electrode is discretized into fine meshes, and each mesh is assigned slightly different porosity and CSA values. The porosity and CSA values are chosen based on the overall properties and standard deviations at the macroscopic level. However, the model uses a mean field approach and does not explicitly consider interconnectivity of pores, or pore size distribution (PSD). As such, the importance of transport and changes in the mesostructure during the cell operation can be overlooked.

To investigate the effect of pores interconnectivity on the electrochemical performances of carbon electrodes, we developed a pore network model (PNM), which enables us to calculate transport properties and simulate electrochemical reactions in three-dimensional (3D) porous structures. A 3D structure of Super P-type carbon is obtained from TXM (transmission X-ray microscopy) nanocomputed tomography with phase contrast imaging using synchrotron X-ray source (APS-ANL). The 3D reconstructed structure allows us to generate porous structures with realistic porosities and pore interconnectivities. Using this model and porous structures, we show that, without altering the mesh porosity or the CSA, mesoscopic differences in the porous cathodes, namely, the pores interconnectivity and the dynamics of pore clogging upon cell discharge, can also lead to a dispersion of the electrochemical performances.

The calculation of model discharge curves is made here following several steps as shown in Figure 1. The initial step is experimental and consists in preparing a porous carbon electrode made of Super P carbon. Prior to the thresholding treatment (using FIJI and AMIRA) to make the segmentation and convert the image stack into a binary file, the tomogram (3000 projections) was properly reconstructed using the Tomopy Python script.²¹

Then, the void (pore) space in the tomography data is mapped to spherical and cylindrical pores using the maximal ball approach,²² and a 3D pore network is extracted. We then simulate a Li–O₂ battery using the PNM approach on the extracted 3D pore network.

For the pore network extraction, an open source code developed by Dong et al. is utilized and adapted to the current system.²³ To extract the pore network, a pore is assigned to each void voxel of the tomography data and expanded until a carbon site is reached. After that an iterative process is carried out to identify the clusters of overlapping pores, which are also called *pore families*, connected by bottlenecks (see Supporting Information for details).

After identifying pore families (two are shown in Figure 2a), only two parameters need to be defined: an effective pore radius for each pore family and the length of the throats that connect these effective pores. To assign these parameters, we use a different approach from the one reported by Dong et al.²³ They use a parameter called the pore-throat segmentation coefficient (α) to determine the effective pore radius and throat length. To calculate the radii of the effective pores, the distances between the center of the *parent pores* and the bottleneck pore (l_i^t and l_j^t) are calculated (Figure 2b) and the radii of the effective pores are given by

$$l_i = l_i^t \left(1 - \alpha \frac{r_t}{r_i} \right) \quad (1)$$

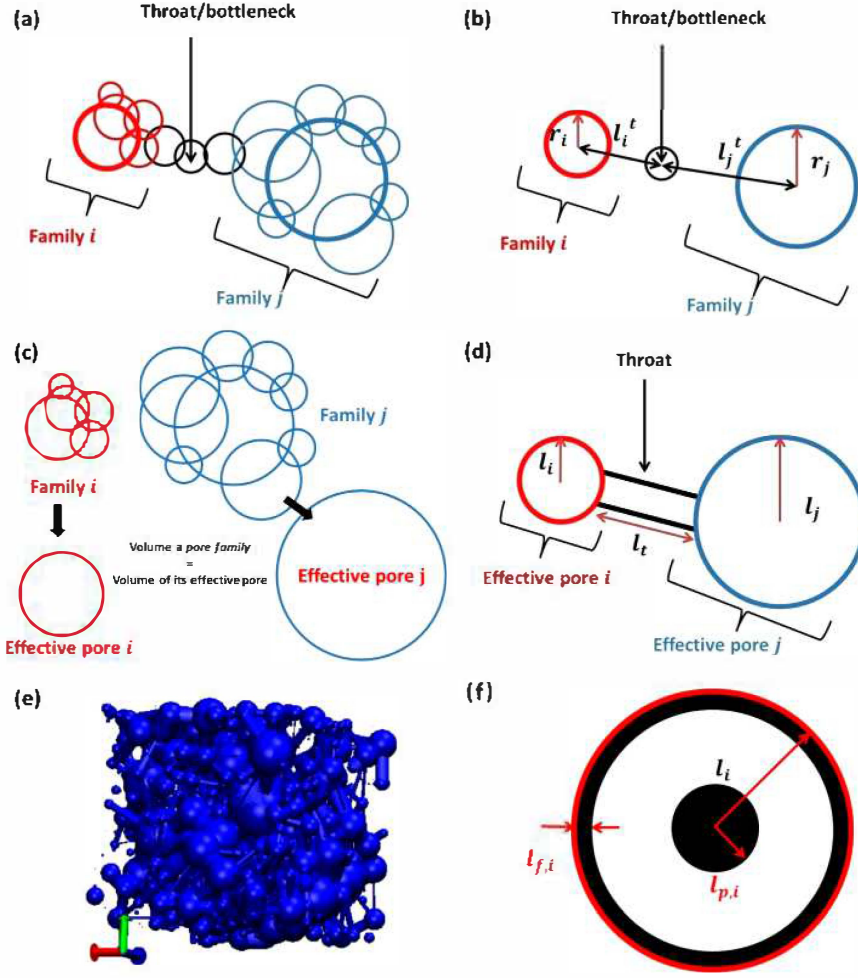


Figure 2. (a–d) Schematic illustrations of the pore network extraction. (a) Two pore families connected via a bottleneck. (b) Dong et al. approach to define effective pore radii and throat lengths.²³ (c) Approach used in this work to assign effective pore radii. (d) Effective pores and throat obtained after assigning effective pore radii and throat lengths either by approaches b or c. (e) Final pore network obtained using the pore network extraction. (f) Illustration of the two mechanisms considered for Li_2O_2 (in black) growth in our model: particle and thin film formation.

$$l_j = l_j^t \left(1 - \alpha \frac{r_t}{r_j} \right) \quad (2)$$

$$l_t = l_{ij} - l_i - l_j \quad (3)$$

where l_p , l_p , and l_t are radii of the effective pore for pore family i , j and the length of the throat, (Figure 2d), r_i is the radius of the throat; r_i is the radius of the parent pore for pore family i ; l_{ij} is the distance between centers of parent pores i and j . This method has two caveats; first, it uses a fitting parameter α and second, it can assign more than one effective radius for a pore family depending on the number of throats it has. We amended this method to assign the effective pore radius (l_i) so that the volume of the effective pore is equal to the total volume of the pore family (Figure 2c). A 3D pore network is then obtained (Figure 2e).

The resolution of X-ray tomography (20 nm voxel size in this work) cannot capture nanopores, and the capacity contribution from those pores is neglected here. We note that experiments on activated carbons, for which the high surface area largely originates from nanopores, do not report high capacities.^{5,24} This is presumably because these pores are readily blocked.

However, this issue with acquiring the 3D structure through experiments can be bypassed via in-silico structure generation, and does not restrict the capability of our model.

The transport equations for the PNM are adapted from the polymer electrolyte membrane fuel cell work of Fazeli et al.²⁵ The evolution of the concentration in each pore is calculated by solving the balance eq 4, written in terms of the fluxes between neighboring pores

$$\frac{dc_{i,x}}{dt} = \sum_j^{\text{neighbours}} k_{ij,x} (c_{j,x} - c_{i,x}) + s_{i,x} \quad (4)$$

where $c_{i,x}$ is the concentration of mobile species x (Li^+ or O_2) in the pore i , and $c_{j,x}$ is the concentration in the pores connected to i . $k_{ij,x}$ is the transfer parameter between pores i and j , and $s_{i,x}$ is the sink term for species x , which is calculated by the electrochemical reactions taking place in pore i . $k_{ij,x}$ is a function of the bulk diffusion coefficient of x ($D_{0,x}$), the distance between the centers of pores i and j , and the cross-sectional areas of pores i , j and the connecting throat, which are A_p , A_j , and A_t respectively, and can be formulated as

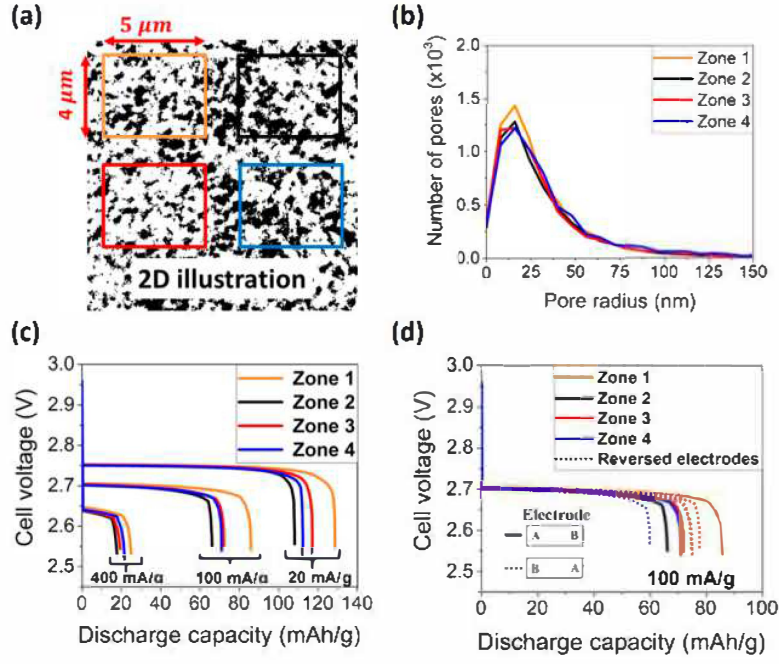


Figure 3. (a) Illustration of the 4 zones taken from the tomography data. (b) PSDs corresponding to the four slices. (c) Calculated discharge curves for the four slices at three different applied current densities. (d) Calculated discharge curves for the flipped electrodes (A: separator side; B: air inlet side).

$$k_{ij,x} = \left(\frac{1}{k_{i,x}} + \frac{1}{k_{j,x}} + \frac{1}{k_{t,x}} \right)^{-1} \quad (5)$$

$$k_{i,x} = \frac{A_i D_{0,x}}{l_i} \quad (6a)$$

$$k_{j,x} = \frac{A_j D_{0,x}}{l_j} \quad (6b)$$

$$k_{t,x} = \frac{A_t D_{0,x}}{l_t} \quad (6c)$$

The cross-sectional areas are calculated by

$$A_i = \pi[(l_i - t_{f,i})^2 - t_{p,i}^2] \quad (7a)$$

$$A_j = \pi[(l_j - t_{f,j})^2 - t_{p,j}^2] \quad (7b)$$

$$A_t = \pi[(r_t - t_{f,t})^2 - t_{p,t}^2] \quad (7c)$$

$t_{f,i}$ and $t_{p,i}$ are the thickness of the Li_2O_2 thin film and the radius of the Li_2O_2 particle formed in the pores considered (Figure 2f). The transport coefficients calculated here neglect the electromigration. This assumption seems reasonable as the discharge capacity is mainly limited by the O_2 (neutral-charge) transport.

The electrochemical discharge reaction generally does not happen in a single step but can involve several intermediate steps such as the formation of superoxides (LiO_2).^{26,27} In this work, for simplicity reasons, an overall reaction is considered



The associated electrochemical reaction rate is formulated as

$$v = k_f a_{\text{Li}^+}^2 a_{\text{O}_2} \exp\left(\frac{-\beta n F (U - U_0)}{RT}\right) - k_b a_{\text{Li}_2\text{O}_2} \exp\left(\frac{(1 - \beta) n F (U - U_0)}{RT}\right) \quad (9)$$

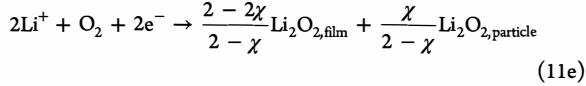
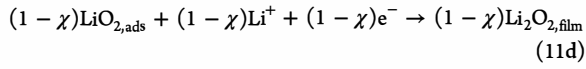
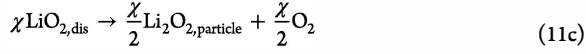
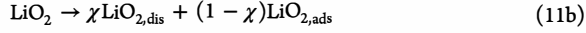
where k_f and k_b are the forward and backward reaction rate constants; a refers to the activities of Li^+ , O_2 , and Li_2O_2 respectively; β is the charge transfer coefficient, n is the number of electrons involved in the electrochemical reaction, U is the electrostatic potential of the electrode, and U_0 is the standard potential of the reaction; R is the universal gas constant, T is the temperature, and F is Faraday constant. The cell potential U is calculated by equating the sum of all currents from all the pores in the network to the input current density or discharge current (I_{tot})

$$I_{\text{tot}} = \sum_{i=1}^{\text{All pores}} S A_i F v \quad (10)$$

where $S A_i$ is the surface area of pore i , which can be either a spherical or a cylindrical pore with the surface area being considered accordingly.

The discharge products can follow two types of pathways: the formation of large particles and the deposition of a thin film. Experimentally, the Li_2O_2 formation path depends on several parameters, such as the electrolyte used,²⁸ the current density²⁹ and the presence of impurities (e.g., the H_2O content in the electrolyte enhancing the LiO_2 solubility).³⁰ In our model, both the formation of large particles and the deposition of a thin film are considered using the escape function concept reported in our previous work.³¹ The escape function is the probability of LiO_2 to escape or dissolve in the electrolyte once it is formed close to the carbon surface. The dissolved LiO_2 is assumed to follow a solution phase mechanism leading to the

formation of large Li_2O_2 particles, whereas the LiO_2 molecules adsorbed on the carbon surface lead to thin film formation. The discharge reaction, including the escape function (χ), can be represented by eqs 11a to 11d, and the amounts of Li_2O_2 particles and thin films (eq 11e) can be calculated by combining these equations:



The escape function values used in this work are given in the [Supporting Information](#).

To investigate the effect of mesostructural differences on the dispersion in electrochemical results and analyze it further, we select four random zones from a single tomography image acquired for a Super P carbon electrode ([Figure 3a](#)) and apply our model to these distinct regions. The active surface areas and porosity values are very close to each other ([Table 1](#)). There is only a difference of about 7% for the porosity and 8% for the CSA. The PSDs are also superimposed ([Figure 3b](#)).

Table 1. Porosities and Specific Surface Areas for the Four Zones

zone number	porosity	surface area
1	0.356	$7.97 \times 10^6 \text{ m}^2/\text{m}^3$
2	0.352	$7.68 \times 10^6 \text{ m}^2/\text{m}^3$
3	0.382	$7.67 \times 10^6 \text{ m}^2/\text{m}^3$
4	0.363	$7.27 \times 10^6 \text{ m}^2/\text{m}^3$

While the four selected regions have similar CSAs, porosities, and PSDs, the discharge curves of these four slices show a significant dispersion of capacities for the three current densities explored ([Figure 3c](#)). The relative differences between the discharge capacities are 29% for $400 \text{ mA}\cdot\text{g}^{-1}$, 23% for $100 \text{ mA}\cdot\text{g}^{-1}$ and 16% for $20 \text{ mA}\cdot\text{g}^{-1}$. These variations in capacities are much larger than the ones for porosity and CSA. To make

sure these differences are not due to slight differences in porosities and CSAs, the four electrodes are flipped; the air inlet and separator sides of the cathode are exchanged. In this case, the macroscopic properties are identical. Yet, the discharge profiles again show variations ([Figure 3d](#)). The main reasons for these large dispersions are inherent to the stochastic nature of the pores interconnectivity and the dynamic change of the porous mesostructure.

For the four selected zones, while the macroscopic properties are similar, the mesoscopic arrangement of pores is not identical, and, in particular, the pores are not connected in the same fashion. In $\text{Li}-\text{O}_2$ batteries, the transport of O_2 and Li^+ in the electrolyte crucially determines the cell capacity, and it is expected that the differences in interconnectivity and pore arrangements will generate a significant dispersion. Besides, unlike in Li-ion batteries, discharge products of $\text{Li}-\text{O}_2$ batteries are solid particles that fill up the porous volume. As such, the porous structure dramatically evolves along the discharge. This is illustrated in [Figure 4](#), which shows the evolution of the pore size distribution along the discharge for zone 2 and the number of inactive pores as a function of time for the same zone in normal and reversed configurations. Once a pore gets clogged, it not only affects itself but also its neighboring pores. This blocks the transport of O_2 and Li^+ to the connected pores through this clogged pore. This can impede long-range transport and also form isolated regions in the pore network that do not contribute to the cell capacity.

[Figure 5](#) shows snapshots of the oxygen concentration at two different depths of discharge for two structures. For the snapshots corresponding to point (a), there are no significant differences of oxygen concentrations in the electrode volume. Yet, for both zones, there are some pores and clusters of pores that are depleted from oxygen, (represented in blue in [Figure 5](#)). These pore clusters are isolated from the oxygen source due to pore/throat clogging. They do not contribute to the cell capacity once they become isolated. This long-range effect explains why pore size distribution evolution is insufficient to explain the discharge capacities observed. Instead, we have to consider all the possible reasons of pore inactivity as given in [Figure S3](#). This is a clear added-value of this model compared to continuum and mean-field computational approaches. This type of features cannot be captured without an explicit description of pores interconnectivity.¹⁷⁻¹⁹ For the color maps of the two zones at point (b), the concentration profiles are very different. This is because along the discharge the

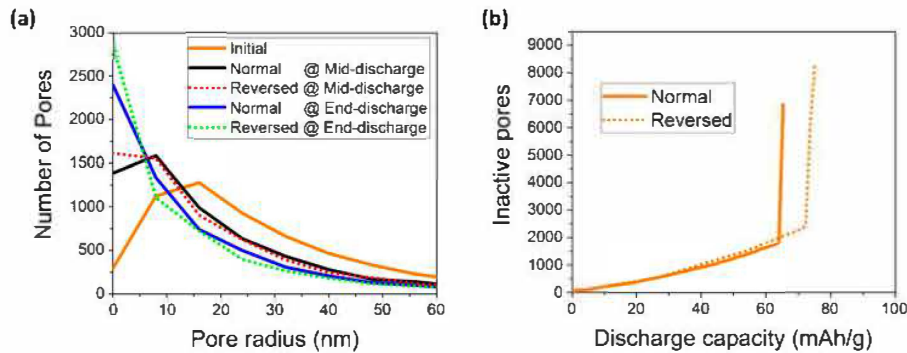


Figure 4. (a) Calculated evolution of PSDs and (b) calculated number of inactive pores along discharge for Zone 2 at $100 \text{ mA}\cdot\text{g}^{-1}$, in normal and reversed configurations. Pores are considered inactive if they are (i) clogged, (ii) passivated by the Li_2O_2 deposit, or (iii) depleted in O_2 (see [Supporting Information](#) for a detailed description of the criteria).

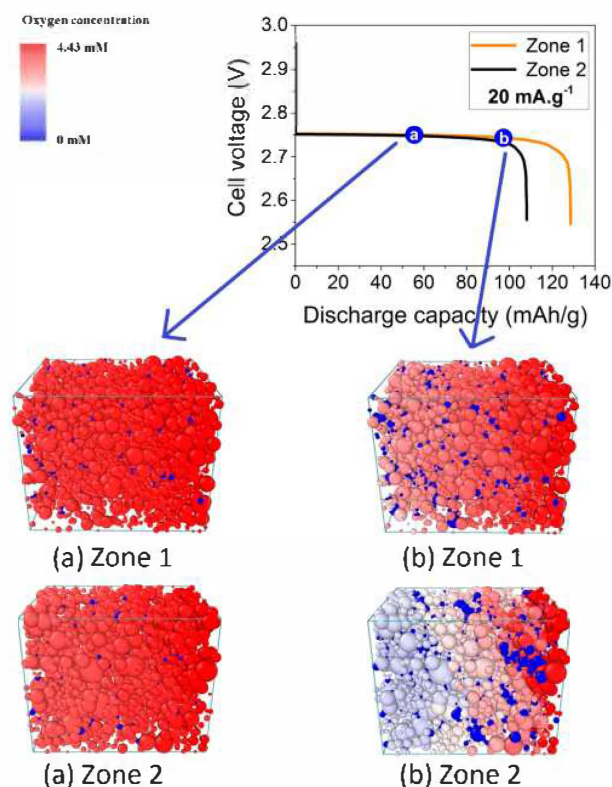


Figure 5. Calculated oxygen concentration color maps at two different depths of discharge, (a) $55 \text{ mAh}\cdot\text{g}^{-1}$ and (b) $97 \text{ mAh}\cdot\text{g}^{-1}$, for two zones at $20 \text{ mA}\cdot\text{g}^{-1}$ discharge current density. Throats (cylindrical pores) are removed for clarity.

porous network evolves due to formation of Li_2O_2 discharge products, and several pores get clogged. For zone 2, there is lack of O_2 transport and a huge gradient of concentration is observed. At this point, the transport of O_2 cannot catch up with the consumption rate, and the cell voltage drops.

In conclusion, we have developed a new model to calculate discharge curves for $\text{Li}-\text{O}_2$ batteries directly comparable with experiments. The model uses tomography images as an input, which allows us to generate a realistic 3D porous structure for which we can simulate the electrochemical performances. To the best of our knowledge, neither the pore network extraction approach nor the PNM have been used so far in the context of $\text{Li}-\text{O}_2$ batteries and batteries in general. Part of the work reported here was focused on adapting these two approaches, already used in other fields, to the case of batteries. With this model, we clearly demonstrate that extra insights can be gained by introducing a 3D representation of porous structures and an explicit description of the pores interconnectivity in modeling works. In particular, we show that the inherent stochastic nature of pores interconnectivity and the mesostructural differences contribute to the dispersion of results observed in experiments. Based on these results, we believe that the variations in the measured capacities/voltages should be reported when presenting experimental discharge curves. This is critically needed to allow comparison of data. Our newly developed model is a useful tool to compare performances of different electrode structures and suggests that structures with less bottlenecks and high porosity will give better electrochemical performance.

EU ASSOCIATED CONTENT

Supporting Information

The Supporting Information is available free of charge on the ACS Publications website at DOI: [10.1021/acs.jpcclett.7b03315](https://doi.org/10.1021/acs.jpcclett.7b03315).

Table of symbols and their descriptions, table of parameters and their values, description of the home-made python script used to convert gray scale tomography images to binary format files, details about the electrode preparation, the tomographic imaging, the procedure followed for electrochemical tests, and additional details about the PNM model, and detailed description and plot of inactive pores and gradient of discharge products along electrode thickness (PDF)

Video showing the calculated oxygen concentration color map along the discharge for a normal electrode (AVI)

Video showing the calculated oxygen concentration color map along the discharge for a reverse electrode (AVI)

EU AUTHOR INFORMATION

Corresponding Author

*E-mail: alejandro.franco@u-picardie.fr.

ORCID

Clare P. Grey: [0000-0001-5572-192X](https://orcid.org/0000-0001-5572-192X)

Alejandro A. Franco: [0000-0001-7362-7849](https://orcid.org/0000-0001-7362-7849)

Notes

The authors declare no competing financial interest.

EU ACKNOWLEDGMENTS

Authors thank Yinghui Yin, Ph.D. student at LRCS Amiens, for preparing the electrode for the tomography imaging. Authors also thank Abbas Shodiev, who was a summer intern student at LRCS Amiens, for discussions on adapting PNM to $\text{Li}-\text{O}_2$ batteries. Authors thank the ALISTORE ERI for A.T.'s Ph.D. funding. A.A.F. acknowledges the Institut Universitaire de France for funding support. C.M. acknowledges the School of the Physical Sciences of the University of Cambridge for funding through an Oppenheimer Research Fellowship. The authors acknowledge the European Union's Horizon 2020 research and innovation programmes for the partial funding support through the POROUS4APP project (Grant Agreement 686163) and through the European Research Council (ERC) (Grant Agreement No 714581). This research used resources of the Advanced Photon Source, a U.S. Department of Energy (DOE) Office of Science User Facility operated for the DOE Office of Science by Argonne National Laboratory under Contract No. DE-AC02-06CH11357. We thank Pr. Martin Blunt and his co-workers, from Imperial College London, for making the original version of the pore network extraction code open source.

EU REFERENCES

- (1) Christensen, J.; Albertus, P.; Sanchez-Carrera, R. S.; Lohmann, T.; Kozinsky, B.; Liedtke, R.; Ahmed, J.; Kojic, A. A Critical Review of Li/Air Batteries. *J. Electrochem. Soc.* **2012**, *159*, R1.
- (2) Abraham, K. M.; Jiang, Z. A Polymer Electrolyte-Based Rechargeable Lithium/Oxygen Battery. *J. Electrochem. Soc.* **1996**, *143*, 1.
- (3) Franco, A. A.; Xue, K. H. Carbon-Based Electrodes for Lithium Air Batteries: Scientific and Technological Challenges from a Modeling Perspective. *ECS J. Solid State Sci. Technol.* **2013**, *2*, M3084–M3100.

- (4) Meini, S.; Piana, M.; Beyer, H.; Schwammlein, J.; Gasteiger, H. A. Effect of Carbon Surface Area on First Discharge Capacity of Li-O₂ Cathodes and Cycle-Life Behavior in Ether-Based Electrolytes. *J. Electrochem. Soc.* **2012**, *159*, A2135–A2142.
- (5) Ding, N.; Chien, S. W.; Hor, T. S. A.; Lum, R.; Zong, Y.; Liu, Z. L. Influence of carbon pore size on the discharge capacity of Li-O₂ batteries. *J. Mater. Chem. A* **2014**, *2*, 12433–12441.
- (6) Xue, K.-H. H.; Nguyen, T.-K. K.; Franco, A. A. Impact of the Cathode Microstructure on the Discharge Performance of Lithium Air Batteries: A Multiscale Model. *J. Electrochem. Soc.* **2014**, *161*, E3028–E3035.
- (7) Kuboki, T.; Okuyama, T.; Ohsaki, T.; Takami, N. Lithium-air batteries using hydrophobic room temperature ionic liquid electrolyte. *J. Power Sources* **2005**, *146*, 766–769.
- (8) Balaish, M.; Kraysberg, A.; Ein-Eli, Y. A critical review on lithium-air battery electrolytes. *Phys. Chem. Chem. Phys.* **2014**, *16*, 2801–2822.
- (9) Bergner, B. J.; Schürmann, A.; Peppler, K.; Garsuch, A.; Janek, J. TEMPO: A Mobile Catalyst for Rechargeable Li-O₂ Batteries. *J. Am. Chem. Soc.* **2014**, *136*, 15054–15064.
- (10) Nasybulin, E.; Xu, W.; Engelhard, M. H.; Li, X. S.; Gu, M.; Hu, D.; Zhang, J. G. Electrocatalytic properties of poly(3,4-ethylenedioxythiophene) (PEDOT) in Li-O₂ battery. *Electrochem. Commun.* **2013**, *29*, 63–66.
- (11) Chen, Y.; Freunberger, S. A.; Peng, Z.; Fontaine, O.; Bruce, P. G. Charging a Li-O₂ battery using a redox mediator. *Nat. Chem.* **2013**, *5*, 489–494.
- (12) Wen, Z.; Shen, C.; Lu, Y. Air Electrode for the Lithium-Air Batteries: Materials and Structure Designs. *ChemPlusChem* **2015**, *80*, 270–287.
- (13) Sun, B.; Huang, X.; Chen, S.; Munroe, P.; Wang, G. Porous graphene nanoarchitectures: An efficient catalyst for low charge-overpotential, long life, and high capacity lithium-oxygen batteries. *Nano Lett.* **2014**, *14*, 3145–3152.
- (14) Yang, W.; Qian, Z.; Du, C.; Hua, C.; Zuo, P.; Cheng, X.; Ma, Y.; Yin, G. Hierarchical ordered macroporous/ultrathin mesoporous carbon architecture: A promising cathode scaffold with excellent rate performance for rechargeable Li-O₂ batteries. *Carbon* **2017**, *118*, 139–147.
- (15) Read, J. Characterization of the Lithium/Oxygen Organic Electrolyte Battery. *J. Electrochem. Soc.* **2002**, *149*, A1190–A1195.
- (16) Griffith, L. D.; Sleightholme, A. E. S.; Mansfield, J. F.; Siegel, D. J.; Monroe, C. W. Correlating Li/O₂ cell capacity and product morphology with discharge current. *ACS Appl. Mater. Interfaces* **2015**, *7*, 7670–7678.
- (17) Ren, Y. X.; Zhao, T. S.; Tan, P.; Wei, Z. H.; Zhou, X. L. Modeling of an aprotic Li-O₂ battery incorporating multiple-step reactions. *Appl. Energy* **2017**, *187*, 706–716.
- (18) Sahapatsombut, U.; Cheng, H.; Scott, K. Modelling the micro-macro homogeneous cycling behaviour of a lithium-air battery. *J. Power Sources* **2013**, *227*, 243–253.
- (19) Yin, Y.; Gaya, C.; Torayev, A.; Thangavel, V.; Franco, A. A. Impact of Li₂O₂ Particle Size on Li-O₂ Battery Charge Process: Insights from a Multiscale Modeling Perspective. *J. Phys. Chem. Lett.* **2016**, *7*, 3897–3902.
- (20) Mehta, M.; Zhu, C.; Andrei, P. Statistical Analysis of Li-Oxygen Batteries. *ECS Trans.* **2017**, *75*, 35–45.
- (21) Gürsoy, D.; De Carlo, F.; Xiao, X.; Jacobsen, C. TomoPy: A framework for the analysis of synchrotron tomographic data. *J. Synchrotron Radiat.* **2014**, *21*, 1188–1193.
- (22) Silin, D.; Patzek, T. Pore space morphology analysis using maximal inscribed spheres. *Phys. A* **2006**, *371*, 336–360.
- (23) Dong, H.; Blunt, M. J. Pore-network extraction from micro-computerized-tomography images. *Phys. Rev. E - Stat. Nonlinear, Soft Matter Phys.* **2009**, *80*, 036307.
- (24) Yang, X. H.; He, P.; Xia, Y. Y. Preparation of mesocellular carbon foam and its application for lithium/oxygen battery. *Electrochem. Commun.* **2009**, *11*, 1127–1130.
- (25) Fazeli, M.; Hinebaugh, J.; Bazylak, A. Incorporating Embedded Microporous Layers into Topologically Equivalent Pore Network Models for Oxygen Diffusivity Calculations in Polymer Electrolyte Membrane Fuel Cell Gas Diffusion Layers. *Electrochim. Acta* **2016**, *216*, 364–375.
- (26) Yin, Y.; Torayev, A.; Gaya, C.; Mammeri, Y.; Franco, A. A. Linking the Performances of Li-O₂ Batteries to Discharge Rate and Electrode and Electrolyte Properties through the Nucleation Mechanism of Li₂O₂. *J. Phys. Chem. C* **2017**, *121*, 19577–19585.
- (27) Belova, A. I.; Kwabi, D. G.; Yashina, L. V.; Shao-Horn, Y.; Itkis, D. M. Mechanism of Oxygen Reduction in Aprotic Li-Air Batteries: The Role of Carbon Electrode Surface Structure. *J. Phys. Chem. C* **2017**, *121*, 1569–1577.
- (28) Johnson, L.; Li, C.; Liu, Z.; Chen, Y.; Freunberger, S. A.; Ashok, P. C.; Praveen, B. B.; Dholakia, K.; Tarascon, J. M.; Bruce, P. G. The role of LiO₂ solubility in O₂ reduction in aprotic solvents and its consequences for Li-O₂ batteries. *Nat. Chem.* **2014**, *6*, 1091–1099.
- (29) Adams, B. D.; Radtke, C.; Black, R.; Trudeau, M. L.; Zaghbi, K.; Nazar, L. F. Current density dependence of peroxide formation in the Li-O₂ battery and its effect on charge. *Energy Environ. Sci.* **2013**, *6*, 1772–1777.
- (30) Aetukuri, N. B.; McCloskey, B. D.; García, J. M.; Krupp, L. E.; Viswanathan, V.; Luntz, A. C. Solvating additives drive solution-mediated electrochemistry and enhance toroid growth in non-aqueous Li-O₂ batteries. *Nat. Chem.* **2015**, *7*, 50–56.
- (31) Xue, K. H.; McTurk, E.; Johnson, L.; Bruce, P. G.; Franco, A. A. A Comprehensive Model for Non-Aqueous Lithium Air Batteries Involving Different Reaction Mechanisms. *J. Electrochem. Soc.* **2015**, *162*, A614–A621.

Supporting information for:

Stochasticity of pores interconnectivity in Li-O₂
batteries and its impact on the variations in
electrochemical performance

Amangeldi Torayev^{1,2,3}, *Alexis Rucci*^{1,4}, *Pieter C. M. M. Magusin*^{2,3}, *Arnaud Demortière*^{1,2,4},
*Vincent De Andrade*⁵, *Clare P. Grey*^{2,3}, *Céline Merlet*^{3,4,6}, *Alejandro A. Franco*^{1,2,4,7,*}

¹ Laboratoire de Réactivité et Chimie des Solides (LRCS), CNRS UMR 7314, Université de Picardie Jules Verne, HUB de l'Energie, Rue Baudelocque, 80039 Amiens, France

² ALISTORE-European Research Institute, Fédération de Recherche CNRS 3104, HUB de l'Energie, Rue Baudelocque, 80039 Amiens, France

³ Department of Chemistry, University of Cambridge, Lensfield Road, Cambridge CB2 1EW, United Kingdom

⁴ Réseau sur le Stockage Electrochimique de l'Energie (RS2E), Fédération de Recherche CNRS 3459, HUB de l'Energie, Rue Baudelocque, 80039 Amiens, France

⁵ X-Ray Science Division, Advanced Photon Source, Argonne National Laboratory, Lemont, USA

⁶ CIRIMAT, Université de Toulouse, CNRS, INPT, UPS, Université Toulouse 3 Paul Sabatier, Bât. CIRIMAT, 118, route de Narbonne 31062 Toulouse cedex 9, France.

⁷ Institut Universitaire de France, 103 Boulevard Saint-Michel, 75005 Paris, France

Experimental methods:

Cathode electrode preparation:

The cathode electrode used for the tomography imaging is made by mixing Super P carbon (Timcal) 90% and PVDF binder 10% weight ratios. The binder and carbon materials are mixed with N-Methyl-2-pyrrolidone (NMP) solvent and dip-coated on a stainless steel mesh. The electrode is dried overnight in a vacuum oven at 110°C.

Tomography imaging:

For the nano-CT (Computed Tomography) measurements, a series of TXM (Transmission X-ray Microscopy) images at different angles are acquired on the beamline 32-ID of the Advanced Photon Source (APS) synchrotron at Argonne National Laboratory. Data set is acquired at energy of 8 keV with 1 s of exposure time per projection in a “flying scan” mode, *i.e.* in continuous rotation. X-ray objective lens is similar to Fresnel zone plate (FZP) and a FZP numerical aperture that matches by the beam shaping condenser, which is a grating with 1.32 mm diameter and 60 nm spacing for the outermost grating. Zernike phase contrast is used to

enhance the contrast of light element (here carbon) using a phase ring localized after the FZP. 1500 projections were acquired along 180° . Pixel is 20 nm large but the true spatial resolution is 60 nm (60 nm features with at least 3 pixels can be seen). Reconstruction is made using Tomopy tools¹⁻³ using the algorithm from the ASTRA toolbox⁴ and accurately approximating algebraic tomographic reconstruction by filtered back projection. As used in previous work,^{5,6} the final 3D reconstructed object is segmented using FIJI and AMIRA software. A part of tomographic image is shown in Figure S1.

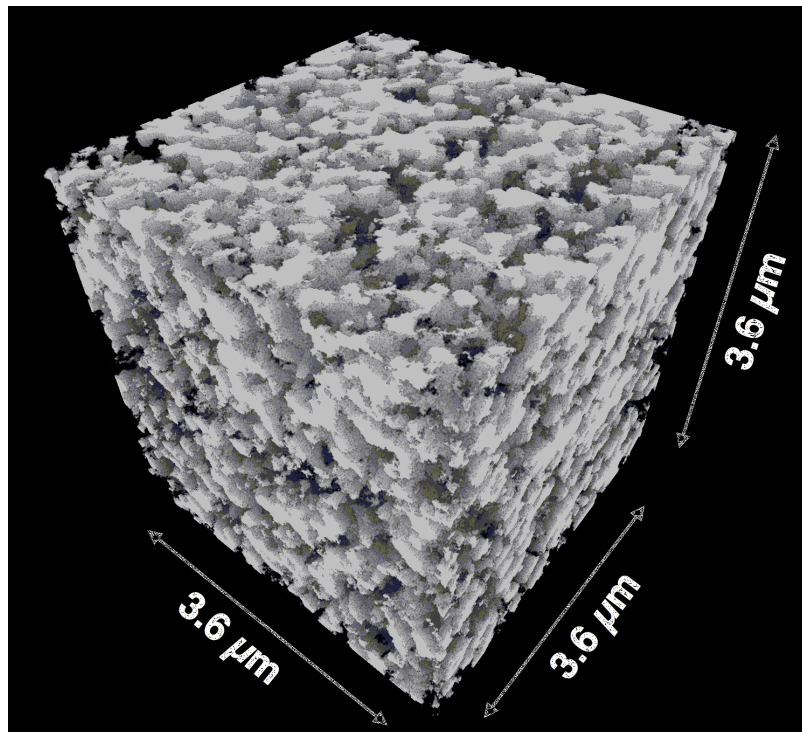


Figure S1. A slice of tomographic image used in this work.

Image processing algorithm:

Tomography data conversion:

A python script is written for the transformation of the tomography grayscale images into a binary file. Each image is divided into pixels, where each one has a gray scale value (or RGB values). In an electrode image stack, a zero gray value represents a pore. This algorithm takes the gray value of each pixel image by image. If it is different from zero it will be represented by '1' in the binary text file, which represents a carbon electrode site. The final file will be a text sequence with a succession of 0 and 1, where each number corresponds to one pixel.

Depending on the quality of the image, segmentation could be needed. In this case the algorithm has to divide the image into two domains (solid part and pore) and then apply the binarization described previously.

Pore network extraction:

After filling up the pore space of the tomography data, an iterative process is carried out to identify the clusters of overlapping pores, connected by bottlenecks. To do that (step 1), the largest pore is taken from the list and assigned as a *parent pore* and all the pores overlapping with that pore are assigned as *child pores*. Then the pores overlapping with the *child pores* are also included as *child pores* of the *parent pore* unless they have a bigger size than the *parent pore*. This process continues till there are no new overlapping pores or the expansion is truncated by larger overlapping pores. This cluster of pores is designated as *pore family i*, where *i* is the index of this *pore family*. All of these pores are removed from the initial list of pores and the process returns to step 1. The process is repeated till all the pores are assigned to a *pore family*.

Computational model:

Initially, we specify the operating conditions (*e.g.* discharge current density, temperature and lithium ion concentration). The pore network simulated in this work contains about 8,000 pores and corresponds to a volume of 5 μm (electrode thickness) x 4 μm x 4 μm . For the PNM, an electrolyte composition of 1M Li^+ ion concentration in TEGDME solvent is considered. A constant oxygen concentration (solubility of O_2 in TEGDME) and zero oxygen flux boundary conditions are applied at the oxygen gas inlet side and at the separator side respectively. For the Li^+ ions, boundary conditions of a constant 1 molar concentration and zero flux are used at the separator side and at the gas inlet end respectively. Periodic boundary conditions are used along the in plane (perpendicular direction to electrode thickness). The initial condition for the model is uniform concentrations of O_2 and Li^+ ions. The code developed is written in C and parallelized. Calculations are carried out on the Odyssey computer cluster owned by the Grey Group. Two nodes with 8 cores each and 2.7 GHz processor speed are used with a RAM of 64 Gb per node.

We simulate an electrochemical reaction leading to the formation of solid Li_2O_2 in both spherical and cylindrical pores. A pore is considered to be blocked when it is filled with discharge products, *i.e.* the thickness of the thin film added to the particle size is equal to the radius of the pore. In this case there can be no reaction in that pore anymore and no transport through it. Additionally, a pore is surface passivated when the thickness of the thin film reaches 10 nm. This is a consequence of the electronic insulator character of the Li_2O_2 . There can be no

electrochemical reaction in a surface passivated pore but it can still contribute to the transport of species.

Table S1. Parameter values used in the model

Parameters	Values	Units	Sources
Physical constants			
Gas constant	8.31	J.K ⁻¹ .mol ⁻¹	<i>universal value</i>
Faraday constant	96485	C.mol ⁻¹	<i>universal value</i>
Cell parameters			
Cathode thickness (Z direction)	5×10 ⁻⁶	m	<i>Defined</i>
Cathode width (X-Y directions) perpendicular to electrode thickness	4×10 ⁻⁶	m	<i>Defined</i>
Li ⁺ initial concentration	1×10 ³	mol.m ⁻³	<i>Assumed</i>
O ₂ initial concentration	4.43	mol.m ⁻³	<i>Ref⁷</i>
Li ₂ O ₂ molar volume	1.98×10 ⁻⁵	m ³ .mol ⁻¹	<i>Ref⁸</i>
Li ⁺ diffusion coefficient	1×10 ⁻¹⁰	m ² .s ⁻¹	<i>Assumed</i>
O ₂ diffusion coefficient	2.17×10 ⁻⁹	m ² .s ⁻¹	<i>Ref⁷</i>
Temperature	298	K	<i>Defined</i>
Electrochemical parameters			
Reaction equilibrium potential	2.96	V	<i>Ref⁹</i>
Charge transfer coefficient	0.5	/	<i>Assumed</i>
Kinetic parameters			
Forward reaction rate constant	1×10 ⁻¹⁰	mol.s ⁻¹ .m ⁻²	<i>Fitted</i>

Backward reaction rate constant	1×10^{-10}	$\text{mol.s}^{-1}.\text{m}^{-2}$	<i>Fitted</i>
Tunneling distance	10	nm	<i>Ref¹⁰</i>

Table S2. List of symbols and their descriptions

Symbol	Description
l_t	Length of a throat or cylindrical pore
l_i	Radius of pore i
r_t	Radius of a throat
l_{ij}	Distance between pore centers of i and j
r_{ki}	Radius of a pore in pore family i
$c_{i,x}$	Concentration of x in pore i
$k_{ij,x}$	Transfer parameter of species x between pore i and j
SA_i	Surface area of pore i
A_i	Cross-sectional surface area of pore i
A_t	Cross-sectional surface area of a throat
$D_{0,x}$	Bulk diffusion coefficient of x
$t_{f,i}$	Thickness of electrochemically grown Li_2O_2 thin film in pore i
$t_{p,i}$	Radius of electrochemically grown large Li_2O_2 particle, also referred as solution phase formation
v	Reaction rate for the electrochemical reaction
k_f	Forward reaction rate constant
k_b	Backward reaction rate constant

a_f	Forward direction activity
a_b	Backward direction activity
β	Charge transfer coefficient
n	Number of electrons involved in the electrochemical reaction
F	Faraday's constant
U	Cell potential
U_0	Standard potential
R	Gas constant
T	Temperature
I_{tot}	Discharge current

Escape function:

The escape function depends on several parameters. Since it contains information about dissolution of LiO_2 intermediate discharge products, every factor related to the LiO_2 solubility also affects the escape function such as the nature of the solvent and additives. On top of these, the discharge rate also influences the formation of large discharge products which can be easily seen on SEM images. The chosen escape function values are similar to the values obtained in our previous work by fitting them to experimental capacities.¹¹ These values are plotted in Figure S2.

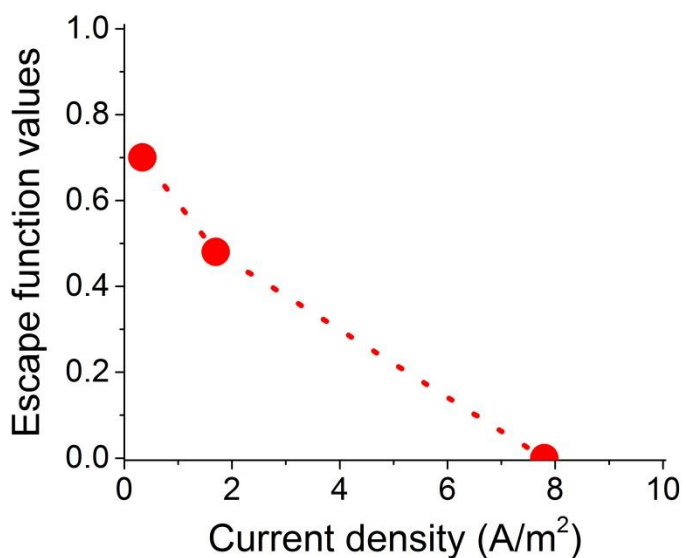


Figure S2. The values of escape function used in this work.

Based on equation 11.e in the main text and the escape function values in Figure S2, the ratios of large particles and thin films are given in the Table S3.

Table S3. Values of escape function and fractions of particle and film formation.

Discharge current	Escape function value	$Li_2O_{2,particle}$ fraction	$Li_2O_{2,film}$ fraction
400 mA.g ⁻¹	0	0	1
100 mA.g ⁻¹	0.48	0.32	0.68
20 mA.g ⁻¹	0.7	0.54	0.46

Results:

A pore is considered inactive if any of the below conditions are met:

1. Clogged: A pore is filled by Li_2O_2 discharge products.
2. O_2 depleted: The concentration of O_2 drops below 0.1 mM . This can happen for two main reasons: i) if neighboring pores are clogged and isolate the pore from the O_2 source (O_2 inlet side) ii) if the transport of O_2 decreases significantly due to change in the electrode mesostructure, and it can't catchup with the O_2 consumption rate.
3. Passivated: The thickness of the thin Li_2O_2 film on the pore surface reaches the tunneling distance limit, 10 nm.

The detailed plot of inactive pores can be seen in Figure S3.

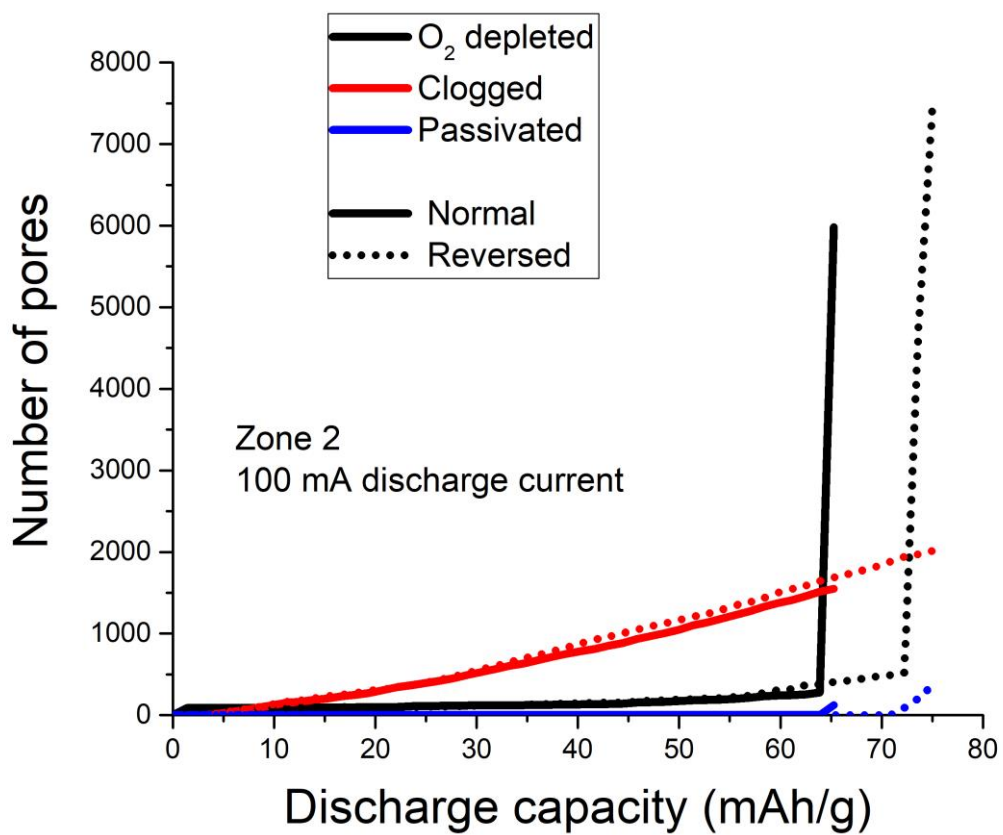


Figure S3. Three types of inactive pores.

The gradient of discharge product along electrode thickness is given in Figure S4. Li_2O_2 forms more on the O_2 inlet side than the separator side.

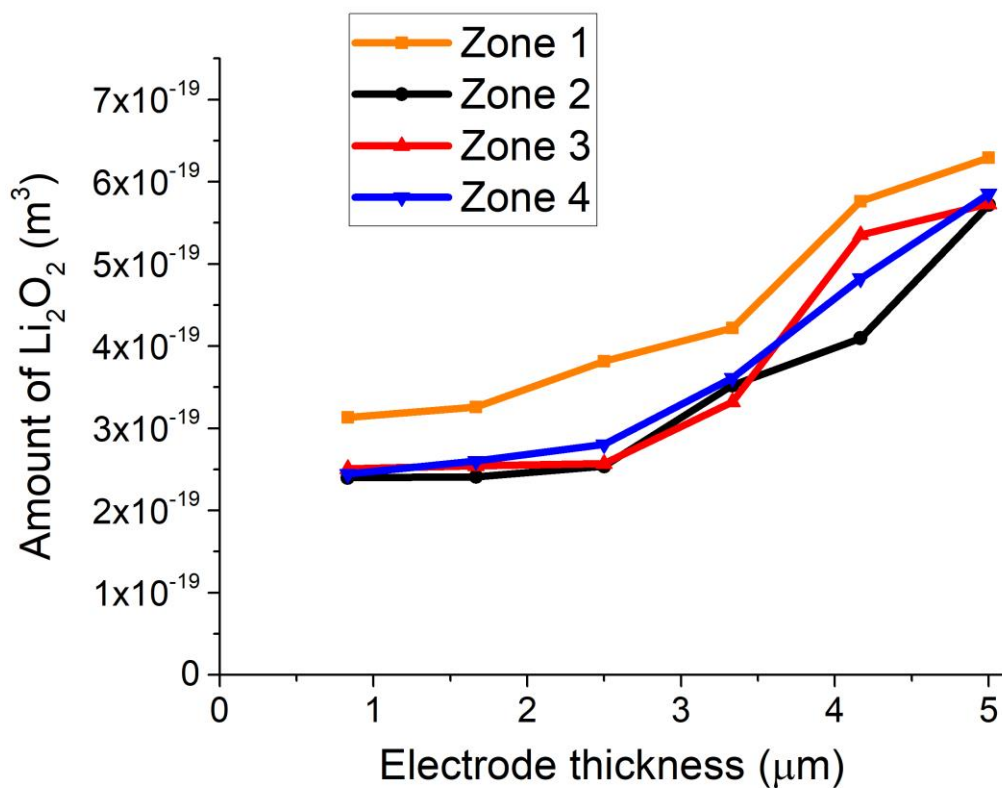


Figure S4. Amount of Li_2O_2 product along electrode thickness for 4 zones at $100 \text{ mA}\cdot\text{g}^{-1}$.

The videos in .avi format correspond to the calculated evolution of oxygen concentration at $100 \text{ mA}\cdot\text{g}^{-1}$ for zone 2 in normal and reversed configurations. The separator/cathode interface is located in the face on the left side.

References:

- (1) Gürsoy, D.; De Carlo, F.; Xiao, X.; Jacobsen, C. TomoPy: A framework for the analysis of synchrotron tomographic data. *J. Synchrotron Radiat.* **2014**, *21*, 1188–1193.
- (2) Miqueles, E. X.; Rinkel, J.; O’Dowd, F.; Bermúdez, J. S. V. Generalized Titarenko’s algorithm for ring artefacts reduction. *J. Synchrotron Radiat.* **2014**, *21*, 1333–1346.
- (3) De Carlo, F.; Gürsoy, D.; Marone, F.; Rivers, M.; Parkinson, D. Y.; Khan, F.; Schwarz, N.; Vine, D. J.; Vogt, S.; Gleber, S. C.; et al. Scientific data exchange: A schema for HDF5-based storage of raw and analyzed data. *J. Synchrotron Radiat.* **2014**, *21*, 1224–1230.
- (4) Pelt, D. M.; Batenburg, K. J. A method for locally approximating regularized iterative tomographic reconstruction methods. **2016**, 1–32.
- (5) Eustache, E.; Douard, C.; Demortière, A.; De Andrade, V.; Brachet, M.; Le Bideau, J.; Brousse, T.; Lethien, C. High Areal Energy 3D-Interdigitated Micro-Supercapacitors in Aqueous and Ionic Liquid Electrolytes. *Adv. Mater. Technol.* **2017**, 1700126.
- (6) Létiche, M.; Eustache, E.; Freixas, J.; Demortière, A.; De Andrade, V.; Morgenroth, L.; Tilmant, P.; Vaurette, F.; Troadec, D.; Roussel, P.; et al. Atomic Layer Deposition of Functional Layers for on Chip 3D Li-Ion All Solid State Microbattery. *Adv. Energy Mater.* **2017**, *7*, 1–12.
- (7) Laoire, C. O.; Mukerjee, S.; Abraham, K. M.; Plichta, E. J.; Hendrickson, M. A. Influence of nonaqueous solvents on the electrochemistry of oxygen in the rechargeable lithium-air

- battery. *J. Phys. Chem. C* **2010**, *114*, 9178–9186.
- (8) Kang, S.; Mo, Y.; Ong, S. P.; Ceder, G. A Facile Mechanism for Recharging Li_2O_2 in Li– O_2 Batteries. *Chem. Mater.* **2013**, *25*, 3328–3336.
- (9) Lu, J.; Amine, K. Recent Research Progress on Non-aqueous Lithium-Air Batteries from Argonne National Laboratory. *Energies* **2013**, *6*, 6016–6044.
- (10) Luntz, A. C.; Viswanathan, V.; Voss, J.; Varley, J. B.; Nørskov, J. K.; Scheffler, R.; Speidel, A. Tunneling and Polaron Charge Transport through Li_2O_2 in Li– O_2 Batteries. *J. Phys. Chem. Lett.* **2013**, *4*, 3494–3499.
- (11) Xue, K. H.; McTurk, E.; Johnson, L.; Bruce, P. G.; Franco, A. A. A Comprehensive Model for Non-Aqueous Lithium Air Batteries Involving Different Reaction Mechanisms. *J. Electrochem. Soc.* **2015**, *162*, A614–A621.